A&A 679, L13 (2023)
https://doi.org/10.1051/0004-6361/202347961

Astronomy & Astrophysics

LETTER TO THE EDITOR

JWST uncovers helium and water abundance variations in the bulge globular cluster NGC 6440

Mario Cadelano[1,2], Cristina Pallanca[1,2], Emanuele Dalessandro[2], Maurizio Salaris[3,4], Alessio Mucciarelli[1,2], Silvia Leanza[1,2], Francesco R. Ferraro[1,2], Barbara Lanzoni[1,2], C.-H. Rosie Chen[5], Paulo C. C. Freire[5], Craig Heinke[6], and Scott M. Ransom[7]

[1] Dipartimento di Fisica e Astronomia "Augusto Righi", Università degli Studi di Bologna, Via Gobetti 93/2, 40129 Bologna, Italy
e-mail: mario.cadelano@unibo.it
[2] INAF-Osservatorio di Astrofisica e Scienze dello Spazio di Bologna, Via Gobetti 93/3, 40129 Bologna, Italy
[3] Astrophysics Research Institute, Liverpool John Moores University, 146 Brownlow Hill, Liverpool L3 5RF, UK
[4] INAF – Osservatorio Astronomico d'Abruzzo, Via M. Maggini, 64100 Teramo, Italy
[5] Max-Planck-Institut für Radioastronomie MPIfR, Auf dem Hügel 69, 53121 Bonn, Germany
[6] Department of Physics, University of Alberta, Edmonton, AB T6G 2G7, Canada
[7] NRAO, 520 Edgemont Road, Charlottesville, VA 22903, USA

Received 14 September 2023 / Accepted 17 October 2023

ABSTRACT

We used ultra-deep observations obtained with the NIRCam aboard the *James Webb* Space Telescope to explore the stellar population of NGC 6440: a typical massive, obscured, and contaminated globular cluster formed and orbiting within the Galactic bulge. Leveraging the exceptional capabilities of this camera, we sampled the cluster down to about five magnitudes below the main sequence turn-off in the (m_{F115W}, $m_{F115W} - m_{F200W}$) colour–magnitude diagram. After carefully accounting for differential extinction and contamination by field interlopers, we find that the main sequence splits into two branches, each above and below the characteristic knee. By comparing the morphology of the colour–magnitude diagram with a suitable set of isochrones, we argue that the upper main sequence bi-modality is likely due to the presence of a He-enriched stellar population with a helium spread of $\Delta Y = 0.04$. The lower main sequence bi-modality can be attributed to variations in the abundance of water (i.e., oxygen) with Δ[O/Fe] ~ -0.4. This is the first evidence of both helium and oxygen abundance variations in a globular cluster purely based on JWST observations. These results open the window for future in-depth investigations of the multiple population phenomenon in clusters located in the Galactic bulge, which were previously unfeasible with near-UV observations, due to prohibitive reddening and crowding conditions.

Key words. globular clusters: general – globular clusters: individual: NGC 6440 – Galaxy: bulge – techniques: photometric – stars: chemically peculiar – infrared: stars

1. Introduction

The existence of multiple stellar populations (MPs) characterised by variations in the abundance of light-elements (such as He, C, N, O, Na, Mg, and Al), while having the same iron-peak content, is a fundamental characteristic observed in virtually all massive and old ($M > 10^4\,M_\odot$, $t \gtrsim 1.5$ Gyr) globular clusters (GCs) within the Milky Way and other galaxies (see, e.g., Bastian & Lardo 2018; Gratton et al. 2019; Piotto et al. 2015; Mucciarelli et al. 2008; Larsen et al. 2014; Dalessandro et al. 2016; Martocchia et al. 2018; Sills et al. 2019; Cadelano et al. 2022). Stars exhibiting light-element abundance ratios resembling those of the surrounding field (i.e., Na-poor/O-rich) are referred to as first-population (FP) stars, while those with Na-rich/O-poor abundances are known as second-population (SP) stars.

The MP phenomenon can be studied through photometry due to the effects that different light-element abundances induce on stellar effective temperatures, luminosities, and spectral energy distributions (e.g., Salaris et al. 2006, 2019; Sbordone et al. 2011; Cassisi & Salaris 2020). These result in splitting or spreads of the evolutionary sequences in the colour–magnitude diagram (CMD) when appropriate filter combinations are adopted (e.g., Piotto et al. 2015; Milone et al. 2017, 2019; Onorato et al. 2023). In this respect, the *Hubble* Space Telescope (HST), with its high-resolution and broad-band capabilities has brought a revolution in the field, significantly enhancing our understanding of the chemical, structural, and kinematic properties of these sub-populations (e.g., Piotto et al. 2015; Milone et al. 2017; Bellini et al. 2015; Dalessandro et al. 2018a, 2019). With the recent launch of the *James Webb* Space Telescope (JWST), a new window of opportunity has opened to further investigate this phenomenon. In fact, as extensively discussed by Salaris et al. (2019, see also Nardiello et al. 2022), JWST filters offer the potential to detect characteristic abundance variations associated with the MPs along both the RGB and the main sequence. Specifically, the near-IR filters employed by the JWST cameras are particularly sensitive to effective temperature variations caused for example by He abundance variations, and to the abundance of water molecules of M-dwarfs (see also Milone et al. 2012, 2019), which correspond to variations in oxygen content, one of the main light elements involved in the MP phenomenon.

Several scenarios have been proposed over the years to explain the formation of MPs, however, their origin is still

debated (see e.g., Bastian & Lardo 2018; Renzini et al. 2022). Exploring the MP phenomenon in different galactic environments may provide valuable insights into the many physical processes contributing to the observed chemical inhomogeneities. In this respect, a systematic mapping of MPs in bulge GCs is still missing due to observational challenges. The combination of severe extinction, crowding and contamination by field interlopers have hindered previous attempts to explore MPs both through spectroscopy of large stellar samples, and through optical-UV photometry. However, bulge GCs constitute a large fraction of the in-situ formed cluster population (Massari et al. 2019), and their MP properties likely retain valuable insights on the environmental conditions in which they were formed.

This Letter presents the first photometric evidence of MPs in NGC 6440 obtained using JWST/NIRcam observations. NGC 6440 is a typical high-mass and metal-rich GC formed and orbiting within the Galactic bulge. Extensive studies of this cluster have revealed a dynamically evolved system, located at 8.3 kpc from the Sun, with a high-mass of $2.7 \times 10^5\,M_{\odot}$, affected by a severe degree of differential reddening ($\delta E(B-V) \sim 0.5$ mag), which evidently distorts the observed evolutionary sequence in the CMDs (Cadelano et al. 2017; Pallanca et al. 2019, 2021; Leanza et al. 2023; Ferraro et al. 2023). The first evidence of MPs in NGC 6440 was found through spectroscopic analysis of seven giant stars by Muñoz et al. (2017). The authors observed intrinsic significant variations in the abundances of Na and Al, while no significant spread in the O abundance was detected.

Here, we demonstrate how the stand-alone exceptional photometric capabilities of the JWST have made possible the detection of MPs in terms of both helium and water abundance variations in such a challenging system representative of the bulge GC population.

2. Data set and data reduction

We used data obtained with the JWST Near Infrared Camera (NIRCam) as part of the GO 2204 program (PI: Freire) conducted during Cycle 1. The data set includes 20 images acquired with the *F115W* filter (Pivot wavelength $\lambda_p = 1.154\,\mu$m), with exposure time of 376 s each and 20 images acquired with the *F200W* filter ($\lambda_p = 1.990\,\mu$m), with an exposure time of 215 s apiece. To complement these observations, we also used the optical data obtained from the Wide Field Camera 3 (WFC3) onboard the HST using a combination of *F606W* and *F814W* filters (see Pallanca et al. 2019, 2021). A detailed and comprehensive description of the specific tools and strategies adopted for the analysis of the observations will be described in detail in a forthcoming paper (Pallanca et al., in prep.). Here, we briefly summarise the main steps. We used DAOPHOT II (Stetson 1987, 1994) to model the point spread function independently for each chip and band and to perform a simultaneous fit to all the sources detected above an appropriate threshold in the JWST and HST observations. The final catalogue includes homogenised magnitudes for all available filters. They were reported to the VEGAMAG photometric system by adopting appropriate zero-points[1] and aperture corrections.

We optimised the proper motion analysis originally presented in Pallanca et al. (2019) to incorporate the new JWST epoch. The calibrated magnitudes were corrected for the heavy degree of differential reddening affecting the field-of-view. This was estimated by using the approach described in Pallanca et al. (2019, see also Cadelano et al. 2020) taking advantage of the NIR-optical filter combination enabled by the simultaneous use of JWST and HST. Briefly, the estimation of differential reddening consisted in two steps. First, we modelled the cluster's mean ridge line using a set of bona-fide cluster members (see Fig. 4 in Pallanca et al. 2019). Then, in the second step, we measured the colour excess variation $\delta E(B-V)$ for each star with respect to the cluster's average value. This measurement consists in determining the shift along the reddening vector (defined using the extinction coefficients by Cardelli et al. 1989; O'Donnell 1994) required to minimise the CMD distance between the mean ridge line and a sample of up to 50 cluster members located within a maximum distance of 5″ from the investigated star. The observed field of view turned to be affected by colour excess variations up to $\delta E(B-V) \sim 0.6$ mag and the resulting differential reddening map is in excellent agreement with the one published by Pallanca et al. (2019), using HST data. We refer to Pallanca et al. (in prep.) for a comprehensive description of both the revised differential reddening correction and the proper motion analysis.

3. Discovery of a dual bi-modal main sequence

To perform a detailed analysis of the CMD features of the cluster, we selected a sample of high-quality and bona fide cluster member stars in the final photometric catalogue. Initially, we excluded stars with photometric errors, chi-square values, and sharpness measurements that exceeded 3σ of the local magnitude values for each filter. Then, we eliminated stars with uncertain differential reddening value according to the residuals of the correction and those located within a distance smaller than the cluster's half-mass radius ($r_{hm} = 50''$; Pallanca et al. 2021). The latter exclusion mitigated potential issues related to blending and saturation that typically arise in the densely populated inner regions of the cluster. Finally, we excluded stars having proper motions larger than three times the dispersion calculated in the corresponding magnitude bin (Fig. 1). The ($m_{F115W}, m_{F115W} - m_{F200W}$) colour–magnitude diagram of the selected sample of stars is shown in Fig. 1 along with the vector-point-diagrams used to remove field interlopers.

The CMD obtained from the JWST observations (see left-hand panel of Fig. 1) extends for more than eight magnitudes and samples the main sequence down to approximately five magnitudes below the turn-off point. Notably, two prominent features are observed along the cluster main sequence. A bi-modal structure in the magnitude range of $20 < m_{F115W} < 21.25$ is observed as two nearly parallel and almost equally populated sequences of stars. Such a bi-modality becomes less evident for magnitudes brighter than $m_{F115W} = 20$ and it disappears around $m_{F115W} = 21.25$. Below the so-called main sequence knee (i.e., at $m_{F115W} > 22$), a second bi-modal pattern becomes apparent in the form of a bluer diagonal sequence and a redder, nearly vertical branch. This double bi-modality feature, observed simultaneously in the same filter combination at magnitudes brighter and fainter than the main sequence knee, provide compelling evidence for the presence of MPs within this cluster.

To analyse the structure of the main sequence in more detail, we verticalised the colour distribution of the stars in the magnitude range $19.7 < m_{F115W} < 21.2$ with respect to two fiducial lines following the blue and red ends of the sequence (see Fig. 2) and calculated as the 5th and 95th percentile of the colour

[1] https://jwst-docs.stsci.edu/jwst-near-infrared-camera/nircam-performance/nircam-absolute-flux-calibration-and-zeropoints#NIRCamAbsoluteFluxCalibrationandZeropoints-NRC_zeropoints

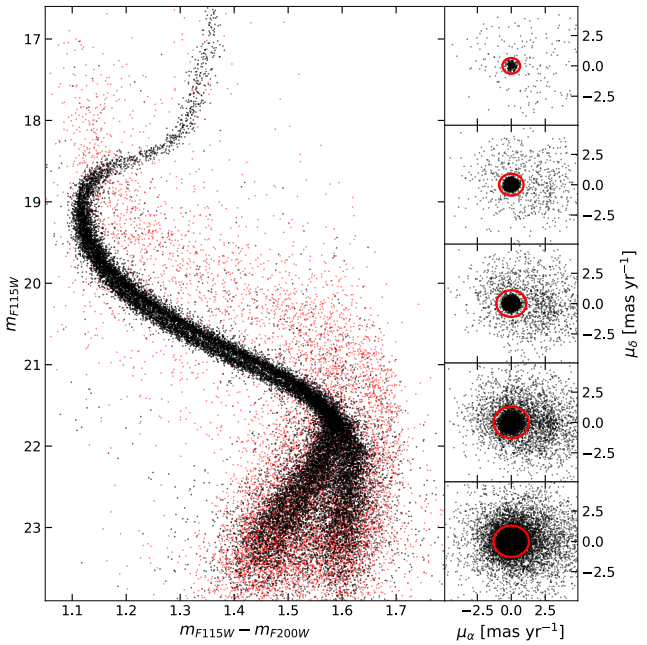

Fig. 1. CMD of NGC 6440 and cluster member selection. *Left-hand panel*: CMD of NGC 6440 obtained with a combination of the *F115W* and *F200W* NIRCam@JWST filters. Black and red dots are high-quality photometry stars flagged as cluster member and field interlopers, respectively. *Right-hand panels*: vector-point-diagram (i.e., proper motion along RA vs. proper motion along Dec) in different magnitude ranges: stars within and beyond the red circles are flagged as cluster members and field interlopers, respectively.

distribution in different magnitude bins (see Dalessandro et al. 2018b for a similar implementation of the technique). The left-hand panel of Fig. 2 displays a zoom on the CMD and the two fiducial lines. The resulting verticalized distribution and its corresponding histogram are presented in the right-hand panels. Notably, the verticalized distribution exhibits two distinct and clearly separated sequences, which are also confirmed by the two strikingly separated peaks in the histogram. We performed a Dip test (Hartigan & Hartigan 1985) and found out that the probability that this colour distribution is uni-modal is lower than 0.5%. To better characterise this bi-modal distribution, we applied a Gaussian Mixture model statistic with two components to fit the histogram of the verticalized colour distribution. The resulting best-fit model is represented by the red and blue curves in the corresponding figure. According to the best-fit analysis, the red sequence includes 4414 stars, while the blue main sequence contains 2913 stars, corresponding to 60% and 40% of the total sample, respectively.

We also investigated the positions of the red and blue sequence stars in the purely optical HST (*F606W*, *F814W*) CMD, which is a classical filter combination mostly sensitive to effective temperature variations. Interestingly, as depicted in Fig. 3, the colour separation between the two sequences is preserved also in this frame, although the separation is smaller and less clearly evident.

To analyse the bi-modality below the main sequence knee and specifically in the magnitude range of $22.2 < m_{F115W} < 23.25$, we applied the same approach discussed above. The results are presented in Fig. 4. The verticalized distribution confirms the presence of at least two prominent and nearly equally populated structures: a blue and diagonal component and a red and almost vertical one. The Dip test yielded a null probability, indicating that the colour distribution is not uni-modal. Fitting the distribution with two Gaussian components, we find that 3124 stars belong to the blue sequence, while 2583 stars belong to the red vertical sequence, corresponding approximately to 55% and 45% of the total sample. It is noteworthy, however, that the blue diagonal component seems to exhibit further substructure. Indeed, two slightly separated structures are discernible, both in the CMD, and in the verticalized colour distribution. In the latter, the separation occurs at $\Delta_{F115W,F200W} = -0.78$ and is robust against variations in the histogram binning. Although the Dip test returns a ∼80% probability that the colour distribution is uni-modal, future observations will hopefully shed light in the possibility that an intermediate sub-population is also present in this cluster. Finally, due to the severe incompleteness and low signal-to-noise ratio (S/N) of the common stars in the HST frame (particularly in the *F606W* filter), a direct comparison in the optical frame is not feasible.

4. Comparison with models

The most plausible explanation of the presence of the two bi-modal distributions observed in this cluster is the co-existence of two stellar populations with different light-element abundances, with the SP composed not only of N-rich/O-poor stars, but also significantly enriched in helium. Above the main sequence knee, variations in nitrogen or oxygen abundance would have a minimal impact on the colours. Therefore, the observed split is more likely a result of effective temperature variations, which are commonly associated with helium and/or iron abundance variations. Assuming that NGC 6440 has no intrinsic metallicity spread (Origlia et al. 2008; Muñoz et al. 2017), the most plausible interpretation is that the observed split in the upper main sequence is indeed caused by a significant difference in the He mass fraction (Y) between the two sub-populations.

On the other hand, the bi-modal split observed at magnitudes fainter than the knee, is probably linked to variations in the abundance of water (i.e., oxygen) on the surfaces of the stars. In fact, the *F200W* filter is particularly sensitive to oxygen abundance variations since it covers a wavelength range where molecular absorptions due to the water molecule fall (Salaris et al. 2019).

To quantify the degree of light-element abundance variations, we compared the observed evolutionary sequences with a set of isochrones. As a reference model, we extracted a BaSTI-IAC isochrone (Hidalgo et al. 2018; Pietrinferni et al. 2021) with an age of 13 Gyr, a distance modulus $(m - M)_0 = 14.65$, an extinction $E(B - V) = 1.26$ (Pallanca et al. 2019, 2021), a metallicity [Fe/H] = −0.6 (Origlia et al. 2008; Muñoz et al. 2017; Crociati et al. 2023)[2], a helium content $Y = 0.257$, and an α-enhanced chemical mixture with $[\alpha/\mathrm{Fe}] = 0.4$, as commonly observed in bulge GCs. Temperature dependent extinction coefficients were calculated following Cardelli et al. (1989) and assuming $R_V = 2.7$ (Pallanca et al. 2021)[3]. This isochrone describes the CMD location of the FP and is depicted as a solid red curve in Fig. 5. It is evident that the model effectively

[2] The adopted metallicity value is 0.05–0.1 dex smaller, than that derived through spectroscopy, but it better reproduces the observed extension and shape of the main sequence. It is worth stressing, however, that all the following results remain unchanged if a metallicity 0.05–0.1 dex larger is adopted.

[3] Please note that a shift by −0.04 mag in the *F115W* was necessary to simultaneously match the evolutionary sequences in all the available filter combinations. Such an offset could be due to uncertainties in the aperture correction, zero points, and encircled energy fractions (see discussion in Sect. 4 of Nardiello et al. 2022).

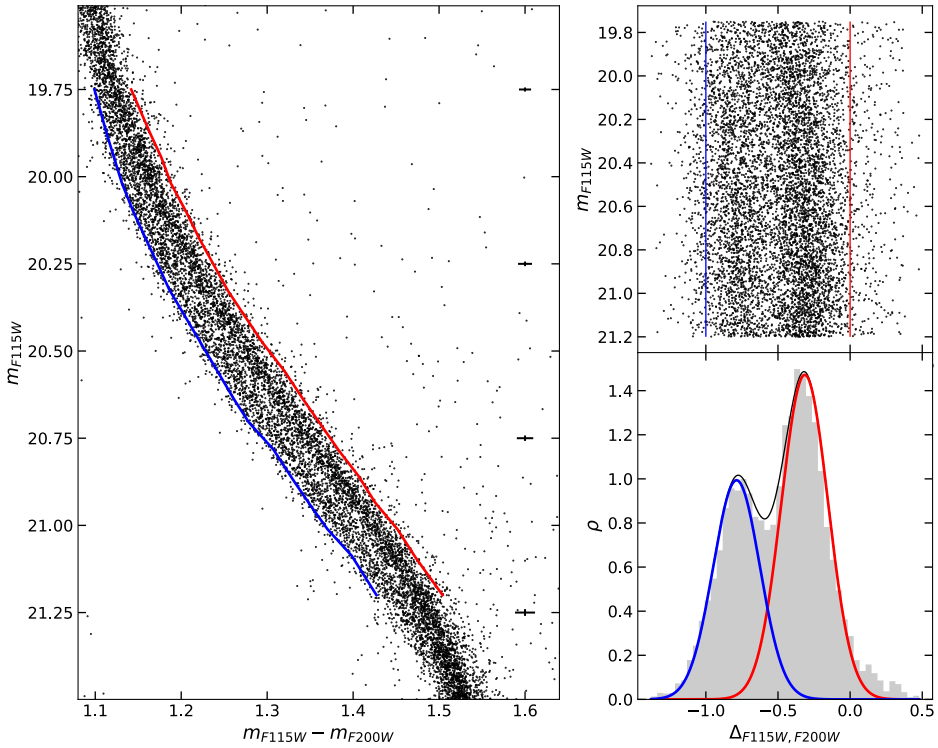

Fig. 2. Upper bi-modality analysis. *Left-hand panel*: JWST CMD of NGC 6440 zoomed on the upper main sequence. The red and blue curves are the two fiducial lines adopted to verticalize the colour distribution. The error bars on the right side on the plot represent the average photometric uncertainties. *Right-hand panels*: verticalized colour distribution of main sequence stars in the magnitude range $19.75 < m_{F115W} < 21.2$, shown in the *top panel*. The *bottom panel* shows the histogram of the same distribution. The blue and red curves display the best-fit Gaussian functions to the observed distribution, while the black one show the sum of them.

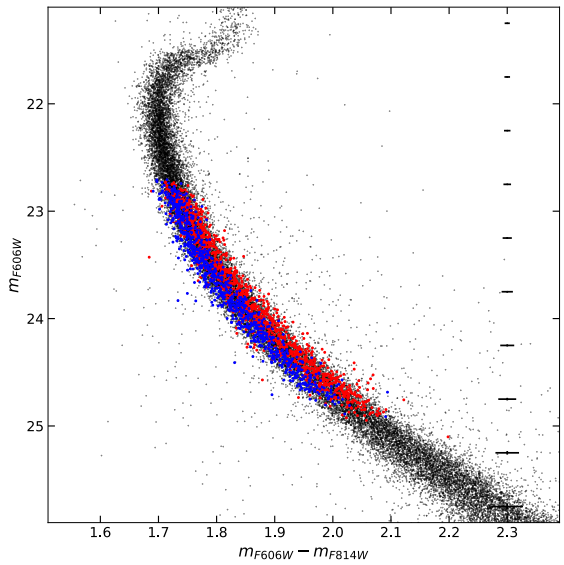

Fig. 3. Optical CMD of NGC 6440 obtained through the combination of the *F606W* and *F814W* filters of the HST/WFC3. Magnitudes are corrected for differential reddening and only bona fide cluster members are plotted. The blue and red stars are those belonging to the blue and red main sequence in the JWST data components selected through the Gaussian mixture model fit (see Fig. 2).

reproduces the evolutionary sequence of the cluster, particularly the red side of the bi-modal upper main sequence and the blue side of the lower main sequence (see also the red solid curve in the right-hand panel of Fig. 5), as expected for an FP with standard He mass fraction. We then extracted a second isochrone with the same properties as the first one but with a higher helium content of $Y = 0.30$. This model (blue line in Fig. 5) aligns well with the observed evolutionary sequence and, specifically, adequately fits the blue side of the upper main sequence. The colour difference between the two isochrones progressively decreases for $m_{F115W} < 20$ and reaches a minimum around the turn-off point, thus naturally explaining the non-detection of the bi-modality in the brighter main sequence portion. Notably, the two models are also capable of explaining the observed width of the red-giant branch, which is significantly larger than expected from the photometric errors. In conclusion, the good match between the observed sequences and the models supports the conclusion that the upper bi-modality is indeed due to helium variations, suggesting an abundance spread of $\Delta Y \approx 0.04$. On the other hand, the helium variation have a negligible impact below the main sequence knee and therefore cannot fully account for the lower bi-modality.

To reproduce the bi-modality observed in the lower main sequence, we computed a set of new isochrones with different choices for the metal distribution, to account for the typical observed anti-correlations among carbon, nitrogen, and oxygen in the SPs. The calculations of the model atmospheres and fluxes followed the procedure described in Hidalgo et al. (2018) using the latest version of the ATLAS9 code. Specifically, we computed spectra and magnitudes for a mildly O-depleted mixture with [O/Fe] = 0.0, [C/Fe] = 0.3, and [N/Fe] = +0.7, as well as a highly O-depleted mixture with [O/Fe] = 0.4, [C/Fe] = 0.6, and [N/Fe] = +1.4 (the C + N + O abundance is kept constant). The FP isochrone and these two new SP isochrones with varying oxygen abundances are shown in the right-hand panel of Fig. 5.

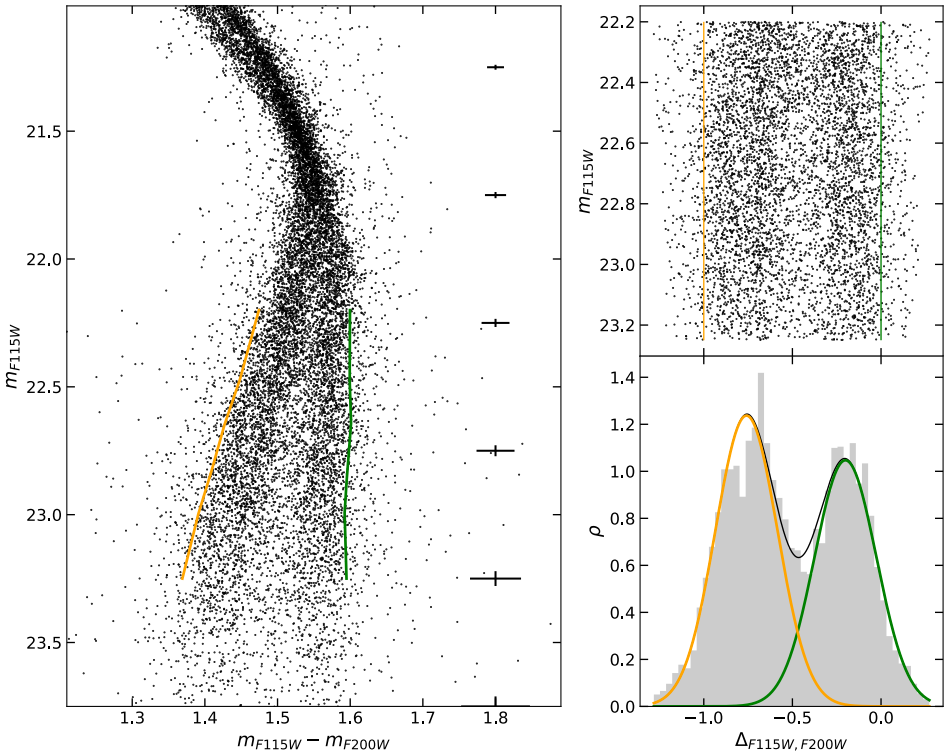

Fig. 4. Lower bi-modality analysis. *Left-hand panel*: JWST CMD of NGC 6440 zoomed on the lower main sequence. The orange and green curves are the two fiducial lines adopted to verticalize the colour distribution. The error bars on the right side on the plot represent the average photometric uncertainties. *Right-hand panels*: verticalized colour distribution of main sequence stars in the magnitude range $22.2 < m_{F115W} < 23.25$, shown at the *top*. The *bottom panel* shows the histogram of the same distribution. The orange and green curves display the best-fit Gaussian functions to the observed distribution, while the black one shows the sum of them.

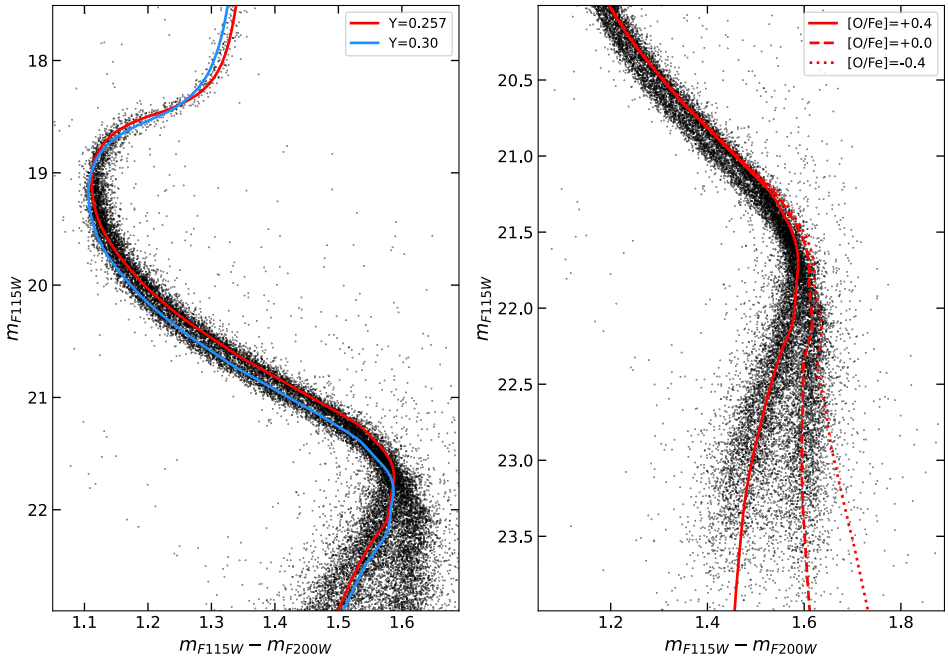

Fig. 5. Comparison of the observed CMD with isochrones. *Left-hand panel*: JWST CMD of NGC 6440 including only bona-fide member stars. The red solid curve is a 13 Gyr BaSTI isochrone reproducing a $[\alpha/\mathrm{Fe}] = +0.4$ stellar population with a metallicity $[\mathrm{Fe/H}] = -0.6$ and a He fraction $Y = 0.257$, representative of the FP. The blue curve is the same model but with a He fraction $Y = 0.30$. *Right-hand panel*: same as the left-hand panel but zoomed on the lower main sequence. The solid curve is the same as in the left-hand panel and reproduces the FP (O/Fe = +0.4), while the dashed and dotted curves are representative of two different SPs with a solar-scaled (O/Fe = +0.0) and (O/Fe = −0.4) oxygen abundance, respectively.

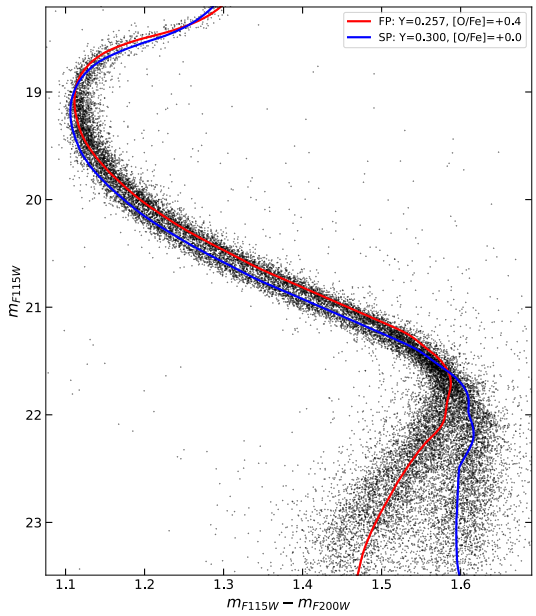

Fig. 6. JWST CMD of NGC 6440 including only bona-fide member stars. The red curve is a 13 Gyr BaSTI isochrone reproducing a [α/Fe] = +0.4 stellar population with a metallicity [Fe/H] = −0.6 and a He fraction Y = 0.257, representative of the FP. The blue curve is an isochrone computed at the same age and metallicity as the previous one, but with a He fraction Y = 0.3 and a solar-scaled (O/Fe = +0.0) chemical mixture, thus making it representative of the SP.

As expected, oxygen variations significantly alter the shape of the isochrones exclusively below the main sequence knee. In particular, it is evident that the isochrone with [O/Fe] = +0.0 effectively matches the red branch of the bi-modal main sequence, while the colours for the [O/Fe] = 0.4 isochrone are too red. These findings suggest the bi-modality below the knee is indeed due to the presence of an O-depleted population with Δ[O/Fe] ∼ −0.4 compared to FP stars. Finally, in Fig. 6 we show the reference FP isochrone alongside an SP isochrone computed assuming a helium rich Y = 0.30 and mildly O-depleted [O/Fe] = 0.0 chemical mixture. It is clear that these two models provide a nice fit to the whole cluster evolutionary sequence, successfully reproducing both the upper and lower bi-modalities.

It is however important to highlight that, as discussed by VandenBerg (2023), the chemical anti-correlations typical of MPs lead to effective temperature offsets among isochrones for very low-mass stars located below the main sequence knee, particularly in the high metallicity regime of NGC 6440 stars. This is due to the effect of an O-depleted metal mixture on the boundary conditions for very low-mass stellar models. These effective temperature offsets are not included in our SP isochrones due to the lack of appropriate boundary conditions with the adopted chemical mixtures in the BaSTI calculations of very low-mass stars. According to Fig. 3 in VandenBerg (2023), the O-depletion results in a higher effective temperature of very low-mass stars, and therefore neglecting this temperature effect implies that the value of Δ[O/Fe] ∼ −0.4 estimated here could be slightly underestimated.

5. Summary and conclusions

This Letter presents the first results of JWST observations of the massive, dense, highly obscured, and highly field-contaminated bulge GC NGC 6440. We used ultra-deep observations acquired with the NIRCam in the *F115W* and *F200W* filters to construct a CMD extending down to ∼5 mag below the main sequence turn-off. By exploiting the synergy with archival HST/WFC3 data, we carefully corrected the CMD for the differential extinction affecting the field of view and disentangled the cluster population from field interlopers through proper motion analysis. This allowed us to obtain the first photometric evidence of MPs in this observationally challenging cluster.

The presence of MPs is observed along the main sequence, which clearly exhibits two distinct and unambiguous bi-modal patterns. One is observed at magnitudes brighter than the main sequence knee (m_{F115W} < 22) and the other at magnitudes fainter than it. A similar behaviour has also been observed using optical and near-IR observations in NGC 2808, a massive GC with extreme MP patterns (e.g., Piotto et al. 2007; Milone et al. 2012).

Above the knee, the main sequence splits into two branches: a red one containing approximately 60% of the stars and a blue one containing the remaining 40%. Through a comparison with a suitable set of isochrones, we demonstrate that this bi-modality is most likely the result of the coexistence of a helium-standard (Y = 0.26) and a helium-enriched stellar population with a difference of $\Delta Y \approx 0.04$. Although further dedicated modelling will be necessary to accurately quantify the helium enrichment history in this cluster, main sequence splits attributed to such phenomenon have been observed in other clusters, s, such as ω Centauri, NGC 2808, and NGC 6441 (Piotto et al. 2007; King et al. 2012; Bellini et al. 2013). Indeed, the existence of heavily helium-enriched stellar populations appears to be a common feature in massive GCs, with the detected helium spreads showing an increasing trend for increasing cluster mass. The estimated helium enrichment is consistent with expectations for a massive cluster like NGC 6440 (Milone et al. 2018), and could also explain its horizontal branch morphology (Mauro et al. 2012).

Below the knee, the main sequence splits again into at least two branches. A similar feature has been already observed among low-mass stars (M-dwarfs) in GCs showing MPs and is likely due to differences in water (i.e., oxygen) abundance (see, e.g., Milone et al. 2019, and references therein). In the case of NGC 6440, the bi-modality consists of a blue branch, likely populated by FP (O-rich) stars, and a red one, likely populated by SP (O-depleted) stars, with the relative fraction of the two population stars being approximately consistent with that estimated above the main sequence knee. The blue sequence appears to be further structured into two sub-sequences. Although this feature currently lacks a statistical confirmation, it could suggest the presence of a more complex MP pattern in this cluster which is worth further investigations in the future. By comparing the observed sequences with a suitable set of isochrones adopting different chemical mixtures typical of MPs, we confirm that the observed bi-modality is due to oxygen variations and we suggest an abundance spread of approximately Δ[O/Fe] ∼ −0.4.

Evidence of MPs below the knee was previously obtained with JWST in the case of M 92 and NGC 104 (Nardiello et al. 2022; Milone et al. 2023). However, a combination of JWST data (acquired with photometric filters different from those used here) and HST optical/near-UV observations has been necessary for the MP characterisation in those clusters. Despite the similar metallicity between NGC 6440 and NGC 104, the present work clearly shows, instead, that the JWST $F115W - F200W$ filter combination is able to unveil the presence of MPs both above and below the main sequence knee, producing a striking bi-modal colour distribution, with no need of additional HST photometry. This highlights the stand-alone effectiveness

of these two JWST filters in discriminating MPs. The results presented in this Letter demonstrate how the superb capabilities of the JWST can be exploited to systematically map the MP phenomenon in observationally challenging clusters, such as those located in the Galactic bulge. Such a mapping was not feasible through spectroscopy of large star samples or near-UV (or even optical) observations and holds the potential to investigate the MP phenomenon in a different chemical and dynamical environment mostly populated by in situ formed GCs.

Acknowledgements. C.-H.R.C. acknowledges support from the Deutsches Zentrum für Luft- und Raumfahrt (DLR) grant NS1 under contract no. 50 OR 2214. M.C., C.P., E.D., S.L., F.R.F and B.L. acknowledge financial support from the project Light-on-Dark granted by MIUR through PRIN2017-2017K7REXT. M.S. acknowledges support from The Science and Technology Facilities Council Consolidated Grant ST/V00087X/1. C.H. is supported by NSERC Discovery grant RGPIN-2023-04264. This research is part of the project Cosmic-Lab (Globular Clusters as Cosmic Laboratories) at the Physics and Astronomy Department A. Righi of the Bologna University (http://www.cosmic-lab.eu/Cosmic-Lab/Home.html).

References

Bastian, N., & Lardo, C. 2018, ARA&A, 56, 83
Bellini, A., Piotto, G., Milone, A. P., et al. 2013, ApJ, 765, 32
Bellini, A., Renzini, A., Anderson, J., et al. 2015, ApJ, 805, 178
Cadelano, M., Dalessandro, E., Ferraro, F. R., et al. 2017, ApJ, 836, 170
Cadelano, M., Saracino, S., Dalessandro, E., et al. 2020, ApJ, 895, 54
Cadelano, M., Dalessandro, E., Salaris, M., et al. 2022, ApJ, 924, L2
Cardelli, J. A., Clayton, G. C., & Mathis, J. S. 1989, ApJ, 345, 245
Cassisi, S., & Salaris, M. 2020, A&A Rev., 28, 5
Crociati, C., Valenti, E., Ferraro, F. R., et al. 2023, ApJ, 951, 17
Dalessandro, E., Lapenna, E., Mucciarelli, A., et al. 2016, ApJ, 829, 77
Dalessandro, E., Cadelano, M., Vesperini, E., et al. 2018a, ApJ, 859, 15
Dalessandro, E., Lardo, C., Cadelano, M., et al. 2018b, A&A, 618, A131
Dalessandro, E., Cadelano, M., Vesperini, E., et al. 2019, ApJ, 884, L24
Ferraro, F. R., Lanzoni, B., Vesperini, E., et al. 2023, ApJ, 950, 145
Gratton, R., Bragaglia, A., Carretta, E., et al. 2019, A&ARv, 27, 8
Hartigan, J. A., & Hartigan, P. M. 1985, Ann. Stat., 13, 70
Hidalgo, S. L., Pietrinferni, A., Cassisi, S., et al. 2018, ApJ, 856, 125
King, I. R., Bedin, L. R., Cassisi, S., et al. 2012, AJ, 144, 5
Larsen, S. S., Brodie, J. P., Grundahl, F., & Strader, J. 2014, ApJ, 797, 15
Leanza, S., Pallanca, C., Ferraro, F. R., et al. 2023, ApJ, 944, 162
Martocchia, S., Niederhofer, F., Dalessandro, E., et al. 2018, MNRAS, 477, 4696
Massari, D., Koppelman, H. H., & Helmi, A. 2019, A&A, 630, L4
Mauro, F., Moni Bidin, C., Cohen, R., et al. 2012, ApJ, 761, L29
Milone, A. P., Marino, A. F., Cassisi, S., et al. 2012, ApJ, 754, L34
Milone, A. P., Piotto, G., Renzini, A., et al. 2017, MNRAS, 464, 3636
Milone, A. P., Marino, A. F., Renzini, A., et al. 2018, MNRAS, 481, 5098
Milone, A. P., Marino, A. F., Bedin, L. R., et al. 2019, MNRAS, 484, 4046
Milone, A. P., Marino, A. F., Dotter, A., et al. 2023, MNRAS, 522, 2429
Mucciarelli, A., Carretta, E., Origlia, L., & Ferraro, F. R. 2008, AJ, 136, 375
Muñoz, C., Villanova, S., Geisler, D., et al. 2017, A&A, 605, A12
Nardiello, D., Bedin, L. R., Burgasser, A., et al. 2022, MNRAS, 517, 484
O'Donnell, J. E. 1994, ApJ, 422, 158
Onorato, S., Cadelano, M., Dalessandro, E., et al. 2023, A&A, 677, A8
Origlia, L., Valenti, E., & Rich, R. M. 2008, MNRAS, 388, 1419
Pallanca, C., Ferraro, F. R., Lanzoni, B., et al. 2019, ApJ, 882, 159
Pallanca, C., Lanzoni, B., Ferraro, F. R., et al. 2021, ApJ, 913, 137
Pietrinferni, A., Hidalgo, S., Cassisi, S., et al. 2021, ApJ, 908, 102
Piotto, G., Bedin, L. R., Anderson, J., et al. 2007, ApJ, 661, L53
Piotto, G., Milone, A. P., Bedin, L. R., et al. 2015, AJ, 149, 91
Renzini, A., Marino, A. F., & Milone, A. P. 2022, MNRAS, 513, 2111
Salaris, M., Weiss, A., Ferguson, J. W., & Fusilier, D. J. 2006, ApJ, 645, 1131
Salaris, M., Cassisi, S., Mucciarelli, A., & Nardiello, D. 2019, A&A, 629, A40
Sbordone, L., Salaris, M., Weiss, A., & Cassisi, S. 2011, A&A, 534, A9
Sills, A., Dalessandro, E., Cadelano, M., Alfaro-Cuello, M., & Kruijssen, J. M. D. 2019, MNRAS, 490, L67
Stetson, P. B. 1987, PASP, 99, 191
Stetson, P. B. 1994, PASP, 106, 250
VandenBerg, D. A. 2023, MNRAS, 518, 4517